

# Theory of Laser-Induced Adiabatic Shaping in Inertial Fusion Implosions: The Decaying Shock

## Introduction

In inertial confinement fusion (ICF),<sup>1</sup> a cryogenic shell of deuterium and tritium (DT) filled with DT gas is accelerated inward by direct laser irradiation (direct drive) or by the x rays emitted by a laser-illuminated enclosure of high- $Z$  material (indirect drive). In the shell frame of reference, the acceleration points from the heavy shell toward the hot ablated plasma, making the shell's outer surface unstable to the well-known Rayleigh–Taylor (RT) instability.<sup>2</sup> In indirect-drive ICF, the high uniformity of the blackbody x-ray radiation results in a negligible level of imprinted perturbations on the shell's outer surface. Indeed, the seeds of the Rayleigh–Taylor instability are mostly provided by the capsule's surface roughness. In direct-drive ICF, the laser-beam intensity is not spatially uniform, and the direct illumination of the shell leads to high levels of laser imprinting that seed the RT instability. The use of random phase plates<sup>3</sup> (RPP's) has successfully shifted the spectrum of laser nonuniformities toward short wavelengths, and the implementation of either smoothing by spectral dispersion<sup>4</sup> (SSD) or induced spatial incoherence<sup>5</sup> (ISI) has provided significant smoothing by modulating the intensity speckle pattern in both space and time. Despite these important advances in smoothing techniques, the current level of imprinting in direct-drive ICF is still sufficiently large to substantially reduce the performance of low-adiabat implosions on the OMEGA laser and high-gain implosions on the National Ignition Facility (NIF).<sup>6</sup>

Since the perturbations seeded by laser imprinting grow exponentially in time during the acceleration phase, it is possible to reduce the RT-induced shell distortion by mitigating the growth rates of the RT instability. The RT growth rates for an all-DT capsule are reduced with respect to the classical value by the well-known ablative stabilization,<sup>7–11</sup> leading to<sup>10</sup>

$$\Gamma \approx 0.94 \sqrt{kg} - 2.7 kV_a, \quad (1)$$

where  $\Gamma$  is the growth rate,  $g$  is the shell acceleration,  $V_a$  is the ablation velocity, and  $k$  is the instability wave number. The

ablation velocity represents the speed of propagation of the heat front inside the shell material and can be defined as the ratio of the ablation rate  $\dot{m}$  and the shell's outer surface (or ablation front) density  $\rho_{\text{out}}$ , leading to

$$V_a = \frac{\dot{m}}{\rho_{\text{out}}}. \quad (2)$$

The ablation rate  $\dot{m}_a$  follows a power law of the laser intensity ( $\dot{m}_a \sim I_L^{1/3}$ ), while the ablation-front density can be written in terms of the shell entropy and ablation pressure  $P_a$ :

$$\rho_{\text{out}} = \left( \frac{P_a}{S_{\text{out}}} \right)^{3/5}, \quad (3)$$

where  $S_{\text{out}}$  is the entropy calculated inside the shell near the ablation front. Using the scaling of the ablation pressure with respect to laser intensity,  $P_a \sim I_L^{2/3}$ , and the definition of the normalized adiabat in DT,  $\alpha \equiv P(\text{Mbar})/2.18 \rho(\text{g/cm}^3)^{5/3}$ , the ablation velocity depends on the laser intensity  $I_L$  and ablation-front entropy:

$$V_a \sim \alpha_{\text{out}}^{3/5} I_L^{-1/15}. \quad (4)$$

Note that  $\alpha \sim S$ . Because of the weak dependence on the laser intensity, one concludes that the ablation velocity depends almost exclusively on the shell adiabat at the outer surface  $\alpha_{\text{out}}$ . In standard target design, the shell entropy is set by the initial strong shock launched when the laser is turned on, yielding a flat-adiabat profile inside the shell. During the acceleration phase, a significant portion of the shell is ablated off, while the remainder coasts inward at a constant velocity once the laser is turned off. When the pressure builds up inside the hot spot, the shell decelerates as its kinetic energy is used to compress both the enclosed hot spot and the shell itself. It is well known that the shell kinetic energy required to compress the hot spot to ignition conditions is roughly proportional to the square of the unablated shell adiabat.<sup>12–14</sup>

$$\varepsilon_K^{\text{ig}} \sim \alpha_{\text{inn}}^2, \quad (5)$$

where  $\varepsilon_K^{\text{ig}}$  is the kinetic energy required for ignition and  $\alpha_{\text{inn}}$  is the normalized adiabat of the inner (unablated) portion of the shell at the end of the acceleration phase. In addition, the energy required to achieve the maximum yield<sup>12</sup> is also a strong function of the in-flight adiabat:

$$\varepsilon_K^{\text{max gain}} \sim \alpha_{\text{inn}}^{1.6 \pm 0.2}, \quad (6)$$

showing that high-adiabat implosions require greater kinetic energy.

In standard ICF target designs, the shell's entropy profile is flat throughout the shell such that  $\alpha_{\text{inn}} = \alpha_{\text{out}}$ . Since large shell adiabats improve stability while lowering the gain, it has been common practice to look for a compromise between stability on the one hand and gain on the other by choosing an intermediate optimized value of the adiabat. It is important to recognize, however, that target gain and stability depend on the local values of the adiabat at different locations in the shell. It follows that high gain and improved stability can indeed be achieved simultaneously by shaping the adiabat inside the shell to maximize the ablation-front adiabat  $\alpha_{\text{out}}$  for better stability and to minimize the inner-surface adiabat  $\alpha_{\text{inn}}$  for higher gain. Though the benefits of adiabat shaping have been recognized by target designers for quite some time, it has not been clear how to implement it. The first mention of adiabat tailoring is in Ref. 15, where it was speculated that adiabat shaping could be induced by the interaction of soft x rays with an ablator material having multiple absorption lines and radiation penetration depths. The first target design<sup>16,17</sup> of radiation-induced adiabat shaping makes use of the x rays produced by a thin gold overcoat and by the carbon radiation in a wetted-foam ablator. Even though such a clever design can produce the desired shaping, significant complications arise from the target-manufacturing aspects, based on wetted-foam technology.

It was later recognized that adiabat shaping can also be induced by modifying the foot of the laser pulse. Two different techniques were proposed: (1) adiabat shaping via a decaying shock (DS)<sup>18</sup> and (2) adiabat shaping via relaxation (RX).<sup>19</sup> Adiabat shaping via a decaying shock relies on the entropy profile left behind by a strong unsupported shock that is launched by an intense laser prepulse. The prepulse is immediately followed by a lower-intensity foot, which slowly evolves into a high-power main pulse. The strong shock launched by

the intense prepulse decays after the laser power is lowered to the foot intensity. As the strong shock starts to decay, it leaves behind a shaped-adiabat profile that has its maximum at the ablation front and minimum on the shell's inner surface. Figure 95.8 shows snapshots of the normalized pressure profile behind a decaying shock (dashed curves) at different times for a 28-Mbar prepulse applied for 75 ps to a DT slab of 100- $\mu\text{m}$  thickness. The solid line represents the adiabat profile left behind by the decaying shock. All the profiles are plotted versus the normalized areal-density coordinate of the foil.

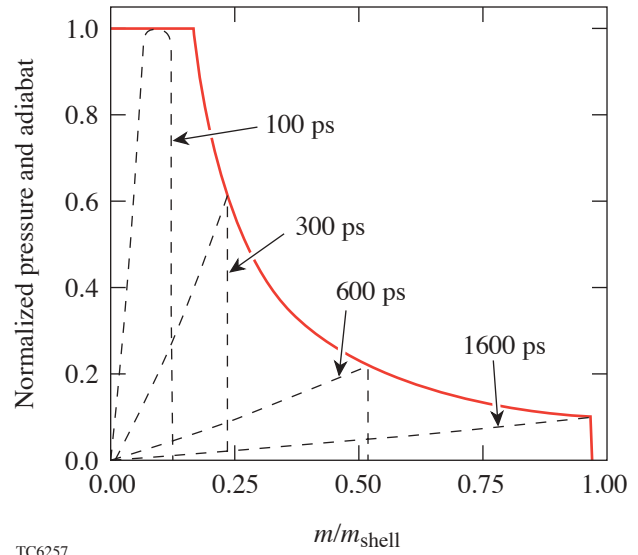


Figure 95.8

Normalized adiabat (solid) near breakout and pressure (dashed) at 100 ps, 300 ps, 600 ps, and 1600 ps for a 75-ps, 28-Mb prepulse.

Adiabat shaping by relaxation also relies on a prepulse launching a decaying shock. The prepulse intensity is much lower, however, than the DS case because the resulting decaying shock is not meant to shape the adiabat but to relax the density and pressure profiles. Indeed, the RX technique requires that the laser power is turned off after the prepulse to allow the shell to decompress and establish relaxed density and pressure profiles. RX adiabat shaping occurs later when the high-intensity foot of the main laser pulse drives a strong shock through the relaxed profiles. As the main shock propagates, it encounters the increasingly larger pressures of the relaxed profiles, causing its strength to decrease, thus leaving behind a shaped-adiabat profile with its maximum at the ablation front and its minimum on the inner surface. Because of the low-power prepulse, the RX technique can be easily implemented

on existing laser systems. Furthermore, the high-power foot of the main pulse leads to a low contrast ratio, better conversion efficiency, and therefore more energy on target.

This article is primarily concerned with a detailed theoretical treatment of laser-induced adiabat shaping by a decaying shock. Here, based on the results of Refs. 18 and 19, we assume that adiabat shaping has a stabilizing effect and focus on the decaying shock evolution. The decaying shock analysis presented here is based on analytical and numerical solutions of the gasdynamic model equations. The adiabat shape is first derived for an ideal case of a shock driven by an applied pressure in the form of a step function in time. The analytic results in the ideal case are derived using an asymptotic matching formula based on a local analysis at the rarefaction–shock interaction point and the asymptotic self-similar solution.<sup>23–28</sup> The ideal adiabat shape reproduces the numerical results very accurately over the entire DS evolution as long as the shock front remains in the strong shock regime. When compared with other theoretical predictions, we find that even though the ideal adiabat shape is in qualitative agreement with Ref. 18, its magnitude is quite different and closer to the standard self-similar solution with an appropriate proportionality constant. The nonideal effects of finite mass ablation and finite residual ablation pressure are evaluated, and the resulting corrections on the adiabat shape are calculated. It is found that the most important correction comes from the residual pressure caused by the finite heat capacity of the coronal plasma, which slows down the ablation-pressure decay when the laser intensity is suddenly lowered. A convenient form of the adiabat shape is derived for carrying out detailed comparisons with the results of full one-dimensional (1-D) simulations using available ICF codes. The agreement between theory and full 1-D simulations is quite remarkable, indicating that the theoretical predictions can be used for target design purposes.

### Lagrangian Hydrodynamics

As is often the case for complicated dynamical problems in gasdynamics, the analysis is greatly simplified by adopting a Lagrangian frame of reference, where the independent spatial coordinate is the mass areal density

$$m = \int_0^x \rho(x', 0) dx'. \quad (7)$$

In this coordinate, the outer shell surface is represented by  $x = 0$  and  $m = 0$ . For simplicity, we calculate for the case of an ideal gas with adiabatic index  $\gamma$  and neglect convergence effects on the basis that the adiabat shaping occurs when the

inner shell surface has not yet moved and the initial aspect ratio is sufficiently large that the shell can be approximated by a uniform slab.

In the Lagrangian frame, the equations of motion for the shocked material can be written in the following conservative form:

$$\frac{\partial u}{\partial m} - \frac{\partial}{\partial t} \frac{1}{\rho} = 0, \quad (8)$$

$$\frac{\partial u}{\partial t} + \frac{\partial p}{\partial m} = 0, \quad (9)$$

$$\frac{\partial}{\partial t} \left( \frac{p/\rho}{\gamma-1} + \frac{u^2}{2} \right) + \frac{\partial}{\partial m} (pu) = 0, \quad (10)$$

governing conservation of mass, momentum, and energy, respectively. In the absence of shocks, the energy equation can be simplified, yielding the isentropic flow condition

$$p = S(m)\rho^\gamma, \quad (11)$$

where  $S(m)$  is referred to as the adiabat or entropy function, which depends exclusively on the Lagrangian coordinate. Equation (11) is valid only for isentropic flow and therefore does not apply across the shock front. At the shock front, the solution of Eqs. (8)–(10) must satisfy the Hugoniot conditions obtained by rewriting Eqs. (8)–(10) in the shock frame of reference and integrating across the shock front. A straightforward calculation leads to the following jump conditions at the shock:

$$\left[ \left| u + \frac{\dot{m}_s}{\rho} \right| \right] = 0, \quad (12)$$

$$\left[ \left| \dot{m}_s u - p \right| \right] = 0, \quad (13)$$

$$\left[ \left| \dot{m}_s \left( \frac{p/\rho}{\gamma-1} + \frac{u^2}{2} \right) - pu \right| \right] = 0. \quad (14)$$

Equations (12)–(14) can be simplified in the strong shock regime, yielding the simple relations for the areal density overtaken by the shock ( $\dot{m}_s$ ), the post-shock density  $\rho_{ps}$ , and velocity  $u_{ps}$ :

$$\rho_{ps} = \frac{\gamma+1}{\gamma-1} \rho_0, \quad (15)$$

$$u_{ps} = \frac{2}{\gamma-1} \frac{\dot{m}_s}{\rho_{ps}}, \quad (16)$$

$$\dot{m}_s = \sqrt{\frac{(\gamma-1)}{2} p_{ps} \rho_{ps}}, \quad (17)$$

where  $p_{ps}$  represents the post-shock pressure. In the sections that follows, Eqs. (8), (9), and (11) and (15)–(17) are solved to determine the dynamics of the shock-induced adiabat shaping.

### The General Problem of the Decaying Shock

Our analysis begins with the study of the propagation of a decaying shock driven by a constant pressure applied over a time interval  $\Delta t_{\text{prep}}$ . At first, we neglect all nonideal effects such as laser ablation and model the laser with a pressure applied on the outer shell surface. The general characteristics of a decaying shock are summarized below.

A uniform strong shock is launched by the ablation pressure  $p_* = P_a^{\text{prep}}$  applied during the prepulse. Here we consider the case of a square prepulse and set  $p_* = \text{constant}$ . This strong prepulse shock compresses the shell material to a density  $\rho_* = \rho_0(\gamma+1)/(\gamma-1)$  (here  $\rho_0$  is the initial shell density) and sets the adiabat of the shocked material to a constant value  $S_* = p_*/\rho_*^\gamma$ . The shock velocity  $U_{s*}$  and the fluid velocity of the shocked material  $u_*$  can be approximated using the Hugoniot relations for strong shocks [Eqs. (15)–(17)], leading to

$$U_{s*} = \sqrt{\frac{(\gamma+1)^2}{2(\gamma-1)} \frac{p_*}{\rho_*}}, \quad (18)$$

$$u_* = \sqrt{\frac{2}{(\gamma-1)} \frac{p_*}{\rho_*}}, \quad (19)$$

where the relation  $U_{s*} = \dot{m}_s/\rho_0$  has been used. After the interval  $\Delta t_{\text{prep}}$ , the laser intensity (and therefore the applied

ablation pressure) is greatly reduced causing a rarefaction wave to propagate from the ablation front toward the shock front. The leading edge of the rarefaction wave travels with the sound speed  $a_* = \sqrt{\gamma p_*/\rho_*}$  inside the shocked material, which in turns travels with the post-shock velocity  $u_*$  with respect to the lab frame. The rarefaction wave's leading-edge velocity in the lab frame is therefore

$$U_r = a_* + u_* = \frac{2}{\gamma+1} \left[ 1 + \sqrt{\frac{\gamma(\gamma-1)}{2}} \right] U_{s*} \quad (20)$$

and is always greater than the shock velocity  $U_{s*}$ , indicating that the rarefaction wave travels faster than the shock. The shock is therefore overtaken by the rarefaction wave. The overtaking time can be determined by equating the distance traveled by the rarefaction wave with the distance traveled by the shock:

$$(u_* + a_*) \Delta t_* = d_c + U_{s*} \Delta t_*, \quad (21)$$

where  $d_c = U_{s*} \Delta t_{\text{prep}} (\gamma-1)/(\gamma+1)$  is the compressed thickness of the shocked material at time  $t = \Delta t_{\text{prep}}$ ,  $a_* = \sqrt{\gamma p_*/\rho_*}$  is the shocked material sound speed, and  $\Delta t_*$  is the traveling time of the rarefaction wave before overtaking the shock. A simple manipulation of Eq. (21) yields the overtaking time interval

$$\Delta t_* = \frac{\Delta t_{\text{prep}}}{\sqrt{2\gamma/(\gamma-1)} - 1}. \quad (22)$$

At time  $t_r = \Delta t_{\text{prep}} + \Delta t_*$ , the shock and the rarefaction wave interact after having propagated through an areal density:

$$m_* = \rho_0 t_r U_{s*} = \Delta t_* \rho_* a_* = \Delta t_* \sqrt{\gamma p_* \rho_*}. \quad (23)$$

Once the shock is overtaken by the rarefaction wave ( $t > t_r$ ), the shock strength starts to decrease, as does the entropy jump across the shock. Since the entropy of each fluid element is conserved after the shock, the adiabat is independent of time and only a function of the areal density:  $S = S(m)$ .

Before the shock starts to decay, the post-shock variables are uniform and their values are denoted by the subscript \*:  $p_*$ ,  $\rho_*$ ,  $S_*$ ,  $a_*$ . Using these post-shock values, one can define a set of dimensionless variables

$$\hat{\rho} \equiv \frac{\rho}{\rho_*}, \quad \hat{p} \equiv \frac{p}{p_*}, \quad \hat{u} \equiv \frac{u}{a_*}, \quad (24a)$$

$$\hat{S} = \frac{S}{S_*}, \quad z = \frac{m}{m_*}, \quad \tau = \frac{t}{\Delta t_*}, \quad (24b)$$

where  $m_*$  and  $\Delta t_*$  are defined in the previous section. Here,  $t = 0$  represents the time when the laser power is lowered and the rarefaction wave is launched. The equations of motion [Eqs. (8), (9), and (11)] can be rewritten in a dimensionless form using the variables in Eqs. (24). A simple manipulation leads to the following form of the equations of motion:

$$\frac{\partial \hat{u}}{\partial z} = \frac{\partial \hat{\rho}^{-1}}{\partial \tau}, \quad (25a)$$

$$\gamma \frac{\partial \hat{u}}{\partial \tau} = -\frac{\partial \hat{p}}{\partial z}, \quad (25b)$$

$$\hat{p} = \hat{S}(z) \hat{\rho}^\gamma, \quad (25c)$$

with the entropy conservation equation [Eq. (25c)] valid away from the shock front. Similarly, the Hugoniot conditions in the strong shock regime can also be written in the following dimensionless form:

$$\dot{z}_s = \sqrt{\frac{\gamma-1}{2\gamma} \hat{S}(z_s)}, \quad (26a)$$

$$\hat{\rho}(z_s, \tau) = 1, \quad (26b)$$

$$\hat{u}(z_s, \tau) = \sqrt{\frac{2\hat{S}(z_s)}{\gamma(\gamma-1)}}, \quad (26c)$$

where  $z_s \equiv m_s(t)/m_*$ . Here the dot in  $\dot{z}_s$  indicates a derivative with respect to  $\tau$ . For  $0 < \tau < 1$ , the rarefaction wave propagates toward the shock front and Eqs. (26) yield the standard rarefaction-wave solution

$$\hat{S} = 1, \quad \hat{p} = \hat{\rho}^\gamma, \quad \hat{\rho} = \left(\frac{z}{\tau}\right)^{\frac{2}{\gamma+1}}, \quad (27a)$$

$$\hat{u} = \frac{2}{\gamma-1} \left[ \left(\frac{z}{\tau}\right)^{\frac{\gamma-1}{\gamma+1}} - 1 \right] + \sqrt{\frac{2}{\gamma(\gamma-1)}}, \quad (27b)$$

where  $z$  varies between 0 and  $\tau$ . At time  $\tau = 1$ , the rarefaction wave overtakes the shock at the point  $z = 1$ . At this time, a perturbation propagating with the sound speed travels backward down the rarefaction wave while the shock strength decays as the shock front travels forward. The adiabat, which is a function of the Lagrangian coordinate  $z$ , is uniform [ $\hat{S}(z) = 1$ ] for  $z < 1$  and decays for  $z > 1$ . For times  $\tau > 1$ , Eqs. (25) need to be solved in the two domains of the rarefaction wave  $0 < z < 1$  and the decaying shock  $1 < z < z_s$ . For  $z < 1$ , the function  $\hat{S}$  is known ( $\hat{S} = 1$ ) while it is unknown for  $z > 1$ . At the point  $z = 1$ , the two solutions must satisfy the boundary conditions of continuous pressure and velocity:

$$\hat{u}(z = 1^-) = \hat{u}(z = 1^+), \quad (28a)$$

$$\hat{p}(z = 1^-) = \hat{p}(z = 1^+). \quad (28b)$$

At the trailing edge of the rarefaction wave ( $z = 0$ ), both density and pressure are small as the applied pressure is greatly reduced after the end of the prepulse. For simplicity, we assume that the post-prepulse pressure is negligible and adopt the vacuum boundary conditions at  $z = 0$ :

$$\hat{\rho}(0, t) = 0, \quad \hat{p}(0, t) = 0. \quad (29)$$

It is important to observe that all the equations and initial and boundary conditions depend only on  $\gamma$ . It follows that the entropy  $\hat{S}(z)$  is a universal function of  $z$  for any given  $\gamma$  and can be determined by a single numerical simulation.

#### Solution for $m \gg m_*$

Even though a single one-dimensional simulation is sufficient to provide the adiabat shape, it is instructive to calculate analytically the entropy distribution. It is important to realize that Eqs. (25) cannot be solved exactly with the boundary and initial conditions in Eqs. (26)–(29). It is, however, intuitive that after some time from the end of the prepulse, the shock propagation becomes independent of initial and boundary conditions and develops a self-similar character. One would expect that the solution of Eqs. (25) becomes self-similar for  $z_s(t) \gg 1$  and  $t \gg 1$ . The self-similar solution has been

studied by several authors<sup>23–28</sup> and provides the asymptotic behavior of a decaying shock. Here we review the self-similar calculation valid for  $z_s \gg 1$  and then solve the decaying-shock problem in the opposite limit of  $z_s(t) \approx 1$  and  $\tau \approx 1$  in order to generate a matching formula approximating the solution for arbitrary  $z$  and  $\tau$ .

A self-similar solution of the decaying-shock problem can be found in the limit of  $m_* \rightarrow 0$ . Because of the absence of characteristic quantities, it is appropriate to use dimensional variables  $m$ ,  $t$ ,  $p$ ,  $\rho$ , and  $u$  and the following divergent form of the entropy:

$$S(m) = \frac{\sigma_*}{m^\delta} \quad (30)$$

with  $\delta$  to be determined by the solvability condition. The shock trajectory can be found from the shock velocity equation [Eq. (17)] after substituting  $p_{ps} = \sigma_* \rho_*^\gamma / m^\delta$  and  $\rho_{ps} = \rho_*$ , leading to the following differential equation:

$$\dot{m}_s(t) = \sqrt{\frac{\gamma-1}{2} \frac{\sigma_* \rho_*^{\gamma+1}}{m_s(t)^\delta}}, \quad (31)$$

which exhibits the power-law solution

$$m_s(t) = \left[ \left( 1 + \frac{\delta}{2} \right) t \sqrt{\frac{\gamma-1}{2} \sigma_* \rho_*^{\gamma+1}} \right]^{\frac{2}{2+\delta}}. \quad (32)$$

Since the only relevant position is the shock location  $m_s(t)$ , the corresponding self-similar coordinate is

$$\xi = \frac{m}{m_s(t)} \quad (33)$$

and the self-similar dependent variables are

$$\rho = \rho_* \hat{\rho}(\xi), \quad u = \frac{\dot{m}_s}{\rho_*} \hat{u}(\xi), \quad p = \sigma_* \rho_*^\gamma \hat{p}(\xi), \quad (34)$$

where  $\hat{p}(\xi) = \hat{\rho}(\xi)^\gamma$ . Substituting Eqs. (33) and (34) into Eqs. (8) and (9) yields the following coupled ordinary differential equations (ODE's) for  $\hat{u}$  and  $\hat{\rho}$ :

$$\pi(\xi) \frac{d\hat{u}}{d\xi} + r(\xi) = 0, \quad (35a)$$

$$\pi(\xi) \frac{\xi}{\hat{\rho}^2} \frac{d\hat{\rho}}{d\xi} + r(\xi) = 0, \quad (35b)$$

where

$$\pi(\xi) = \frac{\gamma-1}{2} \xi - \gamma \frac{\hat{\rho}^{\gamma+1}}{\xi^{\delta+1}}, \quad (35c)$$

$$r(\xi) = \frac{\delta}{4} (\gamma-1) \hat{u} + \delta \frac{\hat{\rho}^\gamma}{\xi^{\delta+1}}. \quad (35d)$$

The boundary conditions at the shock front are governed by the Hugoniot relations

$$\hat{\rho}(1) = 1, \quad \hat{u}(1) = \frac{2}{\gamma-1}, \quad (36)$$

while  $\hat{\rho}(0)$  must vanish [ $\hat{\rho}(0) = 0$ ] since the entropy is infinite at  $m = 0$ . The pressure at  $m = 0$  is not assigned; it is determined instead by the self-similar solution of Eqs. (35). Integrating the momentum conservation equation [Eq. (9)] between  $m = 0$  and  $m = m_s(t)$  and using the Hugoniot relations leads to the following equation for the applied pressure:

$$p(m=0, t) = \frac{\partial}{\partial t} \left[ \int_0^{m_s(t)} u \, dm \right], \quad (37)$$

which can be rewritten upon substitution of Eqs. (32) and (34) into the simple form

$$p(m=0, t) = \frac{1}{\rho_*} \left( \frac{\gamma-1}{2} \sigma_* \rho_*^{\gamma+1} \right)^{\frac{2}{2+\delta}} \times \frac{1-\delta/2}{(1+\delta/2)^{\frac{2\delta}{2+\delta}}} \int_0^1 \frac{\hat{u}(\xi) d\xi}{t^{\frac{2\delta}{2+\delta}}}. \quad (38)$$

Observe that Eq. (38) indicates that the applied pressure is a decaying function of time with a power-law dependence. One

can also argue that the self-similar solution represents the case of an impulsive pressure  $p(m=0, t>0) = 0$  only when the zero global momentum condition is satisfied:

$$\int_0^1 \hat{u}(\xi) d\xi = 0. \quad (39)$$

In summary, the self-similar solution requires either an applied pressure of the form given in Eq. (38) or an impulsive pressure with the condition of zero global momentum [Eq. (39)]. Both the finite-pressure and zero-pressure conditions at  $m=0$  impose some restrictions on the solution of Eqs. (35) near  $\xi \rightarrow 0$ . It is therefore useful to solve the self-similar equation near  $\xi = 0$  to determine whether or not a finite- or zero-pressure solution exists. Indeed, by expanding the equations near  $\xi = 0$ , one finds two power-law solutions:

$$\hat{\rho}(\xi) \approx \Omega_0 \xi^{1+\frac{\delta}{2}} (1 + \Omega_1 \xi^\mu \dots), \quad (40)$$

$$\hat{\rho}(\xi) \approx \theta_0 \xi^{\frac{\delta}{\gamma}} (1 + \nu_1 \xi + \theta_1 \xi^\omega + \dots), \quad (41)$$

where  $\omega = 2 - \delta/\gamma$ ,  $\mu = (\delta + 2)(\gamma - 1)/2$ ,

$$\theta_1 = \frac{1}{\theta_0^{\gamma+1}} \frac{\delta(\gamma-1)}{2\gamma^2\omega(\omega-1)} \left( 1 + \frac{\delta}{2} - \frac{\delta}{\gamma} \right), \quad (42)$$

$$\Omega_1 = \Omega_0^{\gamma+1} \frac{2(\alpha\gamma - \delta)(\alpha\gamma - \delta - 1)}{(\mu - \alpha)\mu} \quad (43)$$

with  $\alpha = 1 + \delta/2$  and  $\theta_0$ ,  $\Omega_0$ , and  $\nu_1$  representing arbitrary constants. It is important to note that Eq. (41) corresponds to the finite-pressure solution while Eq. (40) corresponds to a zero pressure at  $m=0$ .

### 1. Self-Similar Solution

Equations (35) can be numerically solved for different values of  $\delta$ . For  $\delta \leq 1.2748$ , the solution is regular and merges with a constant-pressure solution near  $\xi = 0$ . Figure 95.9 shows a plot of the functions  $\hat{\rho}(\xi)$  and  $\hat{u}(\xi)$  for  $\delta = 1.0$ . Observe that  $\hat{\rho}(0)$  is not zero, representing a solution with a finite applied pressure that decays in time as  $t^{-2\delta/(2+\delta)}$ . In agreement with Ref. 25, the ODE's [Eqs. (35)] become singular for  $\delta = 1.2748$  at the point  $\xi_c \approx 0.0851$ , where  $\pi(\xi_c)$

$= 0$ . Observe that the derivatives of  $\hat{\rho}$  and  $\hat{u}$  would be singular unless  $r(\xi)$  also vanishes at  $\xi_c$ . Indeed, for  $\delta \approx 1.2748$ , both  $\pi(\xi)$  and  $r(\xi)$  vanish at  $\xi_c \approx 0.0851$ , indicating that the derivatives of  $\hat{\rho}$  and  $\hat{u}$  are regular even though they may be discontinuous at  $\xi_c$ . To avoid integrating the equations through the singular point  $\xi_c$ , one can numerically solve between 1 and  $\xi_c$  and between 0 and  $\xi_c$  with the constraint that both  $\hat{\rho}(\xi)$  and  $\hat{u}(\xi)$  be continuous at  $\xi_c$ . The numerical integration in the  $(0, \xi_c)$  interval can be performed by using the expansions in Eqs. (40) and (41) as initial conditions. Indeed, for  $\Omega_0 \approx 1.8949$ , the solution starting from the initial conditions in Eq. (40) matches the solution in  $(\xi_c, 1)$  at the singular point  $\xi_c$ . Similarly, for  $\theta_0 \approx 0.2658$ , the solution starting from the initial conditions in Eq. (41) matches the other solution at  $\xi_c$ , implying that there are two valid self-similar solutions for  $\delta \approx 1.2748$ , corresponding to a finite and to a vanishing applied pressure. Figure 95.10 shows both solutions for  $\delta \approx 1.2748$ . Observe that the two solutions are identical for  $\xi > \xi_c$  and differ in the interval  $(0, \xi_c)$  with the dashed line representing the finite-applied-pressure solution. The existence of two valid solutions for  $\delta = 1.2748$  is quite revealing. Because the finite-pressure solution requires an applied-pressure decaying as

$$p(m=0, t) \sim \frac{1}{t^{\frac{2\delta}{2+\delta}}} \sim \frac{1}{t^{0.78}} \quad (44)$$

and the zero-pressure solution requires a sudden decay, one can speculate that a pressure decay rate faster than  $t^{-0.78}$  does not alter the solution for  $\xi > \xi_c$ , which becomes quickly self-similar with  $\delta \approx 1.2748$ , independent of the applied-pressure

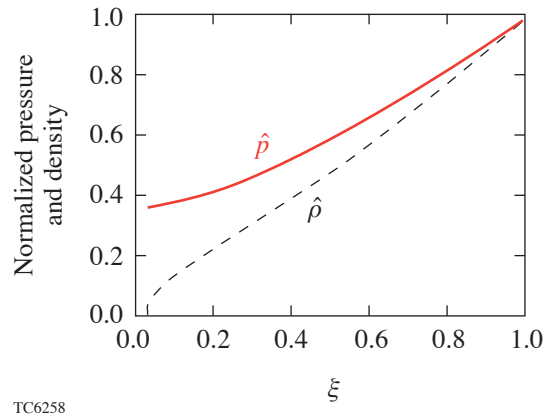


Figure 95.9  
Dimensionless pressure and density as a function of self-similar coordinate for  $\delta = 1.0$ .



$J^+ = 2\hat{a}/(\gamma-1) + \hat{u}$ , which is constant along  $C_1^+$ , yields the following relation for the Riemann invariant:

$$J^+(A) = J^+(B). \quad (49)$$

This equation can be used to determine a relation between  $\hat{u}$  and  $\hat{a}$  at point  $B$ , given these quantities at point  $A$ . The values of both  $\hat{u}$  and  $\hat{a}$  at point  $A$  can be easily determined from the rarefaction-wave solution, leading to

$$\hat{u}_A = \sqrt{\frac{2}{\gamma(\gamma-1)}} - \frac{4d\tau_A}{\gamma+1}, \quad (50)$$

$$\hat{a}_A = \sqrt{\hat{\rho}_A^{\gamma-1}} = 1 - 2\frac{\gamma-1}{\gamma+1}d\tau_A. \quad (51)$$

Since point  $B$  is defined by the coordinates  $z = 1$  and  $\tau = 1 + d\tau$ , the velocity and sound speed can be written as Taylor expansions about the point  $z = 1$ ,  $\tau = 1$ , yielding

$$\hat{u}_B = \hat{u}_{1,1} + \left[\frac{\partial \hat{u}}{\partial \tau}\right]_{1,1} d\tau = \sqrt{\frac{2}{\gamma(\gamma-1)}} + \left[\frac{\partial \hat{u}}{\partial \tau}\right]_{1,1} d\tau, \quad (52a)$$

$$\hat{a}_B = \hat{\rho}_B^{\frac{\gamma-1}{2}} = 1 + \frac{\gamma-1}{2} \left[\frac{\partial \hat{\rho}}{\partial \tau}\right]_{1,1} d\tau. \quad (52b)$$

Substituting Eqs. (50)–(52) into (49) leads to the following relation between the pressure gradient and density time derivative:

$$\left[\frac{\partial \hat{p}}{\partial z}\right]_{1,1} = \frac{4\gamma}{\gamma+1} + \gamma \left[\frac{\partial \hat{\rho}}{\partial \tau}\right]_{1,1}, \quad (53)$$

where the pressure gradient enters Eq. (53) through the momentum conservation equation relating the acceleration to the pressure gradient. It is important to emphasize that all the temporal and spatial derivatives above are calculated at  $z = 1^-$ , which is before the shock decay region ( $z > 1$ ). Because the pressure, entropy, density, and velocity are continuous at  $z = 1$ , it follows that all the time derivatives must also be continuous. Furthermore, the conservation of momentum [Eq. (9)] requires that the pressure gradient be continuous due to the continuity of the acceleration ( $\partial_t u$ ). On the other hand,

there are no such constraints on the density and entropy gradients, which are discontinuous at  $z = 1$ .

The next step is to expand the Hugoniot conditions concerning the post-shock velocity at the shock front defined as  $z_s = 1 + dz_s$ . We start from the post-shock velocity equation

$$\hat{u}(1 + dz_s, 1 + d\tau) = \sqrt{\frac{2}{\gamma(\gamma-1)}} \hat{p}(1 + dz_s, 1 + d\tau) \quad (54)$$

and expand it near (1,1), retaining the first-order terms

$$\left(\frac{\partial \hat{p}}{\partial \tau}\right)_{1,1} \left[ \sqrt{\frac{\gamma}{2(\gamma-1)}} + \sqrt{\frac{\gamma-1}{2\gamma}} \right] + \left(\frac{\partial \hat{p}}{\partial z}\right)_{1,1} \frac{3}{2\gamma} = 0. \quad (55)$$

In the derivation of (55), the equations of motions [Eqs. (25)] and the shock velocity at  $\tau = 1$ ,  $\dot{z}_s(1) = \sqrt{\gamma-1}/2\gamma$  have been used. Equations (53) and (55) can then be solved to determine the density time derivative and the pressure gradient, which depend only on the adiabatic index

$$\left(\frac{\partial \hat{p}}{\partial \tau}\right)_{1,1} = -\frac{6/(\gamma+1)}{\frac{3}{2} + \sqrt{\frac{\gamma}{2(\gamma-1)}} + \sqrt{\frac{\gamma-1}{2\gamma}}}, \quad (56)$$

$$\left(\frac{\partial \hat{p}}{\partial z}\right)_{1,1} = \frac{4\sqrt{2}\gamma(2\gamma-1)}{(\gamma+1) \left[ 3\sqrt{\frac{\gamma}{2(\gamma-1)}} + \sqrt{2(\gamma-1)} + \sqrt{2\gamma} \right]}. \quad (57)$$

The remaining Hugoniot condition concerning the post-shock density  $\hat{\rho}(1 + dz_s, 1 + d\tau) = 1$  can also be expanded to first order and, using Eq. (56), yields the density gradient at  $z = 1$ ,  $\tau = 1$ :

$$\left(\frac{\partial \hat{\rho}}{\partial z}\right)_{1,1}^+ = \frac{6/(\gamma+1)}{\frac{3}{2} \sqrt{\frac{\gamma-1}{2\gamma}} + \frac{1}{2} + \frac{\gamma-1}{2\gamma}}, \quad (58)$$

where the superscript + indicates that the derivative is calculated on the  $z > 1$  side. The last step is to determine the entropy gradient at  $z = 1$  using the definition of the dimensionless entropy  $\hat{S} = \hat{p}/\hat{\rho}^\gamma$  and the pressure and density gradients

provided by Eqs. (57) and (58). A straightforward calculation leads to the following form of the entropy gradient at the beginning of the shock decay:

$$\left(\frac{\partial \hat{S}}{\partial z}\right)_{1,1}^+ = -\beta, \quad \beta = \frac{2\gamma}{2\gamma-1}(1+\epsilon), \quad (59a)$$

where

$$\epsilon = -1 + 2\sqrt{2} \frac{2\gamma-1}{3\sqrt{\gamma(\gamma-1)} + \sqrt{2}(2\gamma-1)}. \quad (59b)$$

For  $\gamma > 1.4$ , the term  $\epsilon$  is typically small ( $|\epsilon| < 0.06$ ) and asymptotically reaches the constant value  $-0.029$  for  $\gamma \rightarrow \infty$ . This concludes the solution near  $z = 1$ . The entropy and its derivatives at  $z = 1$  have been determined and can be used together with the self-similar solution to generate a matching formula approximating the entropy over the entire range of  $z \geq 1$ .

### Matching Formula for the Adiat Shape

An approximate formula representing the entropy profile left behind by a decaying shock can be constructed by matching the solution near  $m = m_*$  with the self-similar behavior for  $m \gg m_*$ . The matching formula must satisfy the conditions

$$\hat{S}(1) = 1, \quad \frac{d\hat{S}}{dz}(1) = -\beta, \quad \hat{S}(z \rightarrow \infty) \sim \frac{0.923}{z^\delta}, \quad (60)$$

where  $\delta = 1.2748$  and  $\beta = 1.459$  for  $\gamma = 5/3$ . It is important to notice that the self-similar solution provides only the scaling with  $z$  but not the actual coefficient. While a coefficient near unity is expected, the numerical solution of the Euler equations [Eqs. (8)–(10)] has indicated that the correct coefficient for ( $\gamma = 5/3$ ) is 0.923. An extremely accurate representation of the adiabat profile can be obtained by choosing the following fitting formula:

$$\hat{S}(z) = \left( \frac{1+\nu}{z^{\delta/\sigma} + \nu} \right)^\sigma, \quad (61)$$

which satisfies the two conditions  $\hat{S}(1) = 1$  and  $\hat{S}(z \rightarrow \infty) \sim z^{-\delta}$ . The parameters  $\nu$  and  $\sigma$  can be determined by applying the other two conditions on  $\hat{S}'(1)$  and on the coefficient 0.923

[Eq. (60)]. A simple calculation leads to the following values (for  $\gamma = 5/3$ ):  $\nu = -0.127$  and  $\sigma = 0.591$ , which upon substitution into Eq. (61) yields the adiabat shape function

$$\hat{S}(z) \approx \left( \frac{0.873}{z^{2.157} - 0.127} \right)^{0.591}. \quad (62)$$

A simpler formula for the adiabat shape can be obtained by fitting Eq. (62) with a simple power law such as

$$\hat{S}(z) \approx \frac{1}{z^{1.315}}, \quad (63)$$

which exhibits an error below 3% with respect to the numerical solution over the range  $1 < z < 10$ . Figure 95.12 shows the ratios between the numerical solution of the Euler equations [Eqs. (8)–(10)] and Eqs. (62) (solid) and (63) (dashed). Observe that Eq. (62) reproduces the numerical results very accurately over any range of  $z$ . Figure 95.12 also shows a comparison between the numerical solution with the adiabat shape derived in Ref. 18 (dashed-dotted) and the self-similar solution  $\hat{S} = z^{-1.275}$  (dotted) of Refs. 23–28. The adiabat profile of Ref. 18, derived using a spatially frozen pressure profile, exhibits a significantly different behavior from Eq. (62), while the behavior of the self-similar solution differs mostly near  $z = 1$ . In view of the good agreement between the simple power law and the simulation, Eq. (63) will be used as

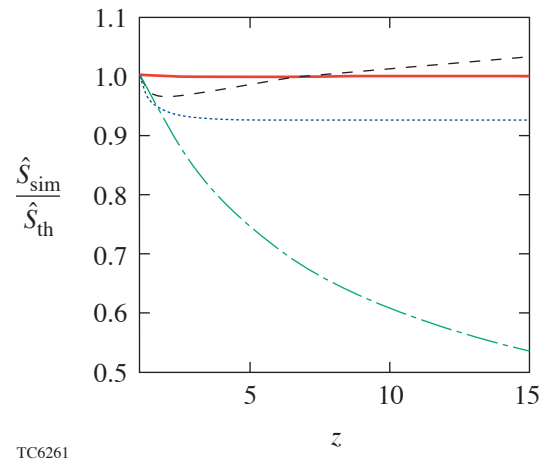


Figure 95.12

Comparison of the numerical solution of Eqs. (8)–(10) to several analytical formulas for the adiabat shape: Eq. (62) (solid); Eq. (63) (dashed); Eq. (4) of Ref. 18 (dashed-dotted); solution from Refs. 23–28 (dotted).

the adiabat shape induced by a decaying shock in an ideal gas when the applied pressure vanishes right after the end of the prepulse.

### Effects of Mass Ablation and Residual Ablation Pressure

In laser-driven implsions, mass is ablated off the outer shell surface at a rate  $\dot{m}_a$ , which depends on the laser intensity  $\dot{m}_a \sim I_L^{1/3}$ . When the laser power is lowered after the prepulse ( $t = \Delta t_{\text{prep}}$ ) and the rarefaction wave is launched, a fraction of the shell mass has been ablated. Since the relevant  $m_*$  is the areal density overtaken by the rarefaction wave before interacting with the shock, it is appropriate to reset the origin of the  $m$  variable so that  $m = 0$  corresponds to the fluid element on the outer surface at the end of the prepulse  $t = \Delta t_{\text{prep}}$ . For this purpose, we denote the new mass variable as  $m^{(a)} = m - m_a^{\text{prep}}$ , where  $m_a^{\text{prep}}$  is the mass ablated during the prepulse and  $m^{(a)} = 0$  represents the point where the rarefaction wave is launched. The time  $\Delta t_*$  representing the time interval between the end of the prepulse and the rarefaction–shock interaction is affected by ablation and satisfies the following equality:

$$(u_* + a_*)\Delta t_* = d_c - d_a + U_{s*}\Delta t_*, \quad (64)$$

where  $d_c = U_{s*}\Delta t_{\text{prep}}(\gamma - 1)/\gamma + 1$  is the compressed thickness of the shocked material at time  $t = \Delta t_{\text{prep}}$  and  $d_a$  is the thickness of the ablated portion  $d_a = m_a^{\text{prep}}/\rho_* = V_a^{\text{prep}}\Delta t_{\text{prep}}$ , where  $V_a^{\text{prep}}$  is the ablation velocity during the prepulse. The interval  $\Delta t_*$  can be derived from Eq. (64), yielding

$$\Delta t_*^a = \frac{\Delta t_{\text{prep}}}{\sqrt{2\gamma/(\gamma-1)} - 1} \left( 1 - \sqrt{\frac{2\gamma}{\gamma-1}} M_a^{\text{prep}} \right), \quad (65)$$

where  $M_a^{\text{prep}} \equiv V_a^{\text{prep}}/a_*$  represents the ablative Mach number during the prepulse. Observe that we have used the superscript  $a$  to discriminate between the  $\Delta t_*$  with [Eq. (65)] and without [Eq. (22)] ablative correction.

It is interesting to notice that  $M_a^{\text{prep}}$  is independent of the laser power. Indeed, using the well-known relations for the ablation rate and pressure,<sup>1,29,30</sup> one can easily construct the following expression:

$$\dot{m}_a \text{ (g/cm}^2 \text{ s)} \approx 5.2 \times 10^5 \left[ \frac{0.35}{\lambda \text{ (}\mu\text{m)}} \right] \left[ \frac{P_a \text{ (Mbar)}}{20} \right]^{0.5}, \quad (66)$$

where  $\lambda$  ( $\mu\text{m}$ ) is the laser wavelength in microns and  $P_a$  (Mbar) is the ablation pressure in megabars. The ablative Mach number is calculated for  $\gamma = 5/3$  by setting  $V_a^{\text{prep}} = \dot{m}_a^{\text{prep}}/\rho_*$ , leading to

$$M_a^{\text{prep}} \approx 0.091 \left[ \frac{0.25}{\rho_0 \text{ (g/cm}^3)} \right]^{0.5} \left[ \frac{0.35}{\lambda \text{ (}\mu\text{m)}} \right], \quad (67)$$

where  $\rho_0$  is the initial density in  $\text{g/cm}^3$  before the shock. Observe that the ablative correction of  $\Delta t_*$  in Eq. (65) is significant and approximately equal to 20% for DT ice ( $\rho_0 = 0.25 \text{ g/cm}^3$ ) and UV lasers ( $\lambda = 0.35 \mu\text{m}$ ) leading to  $\Delta t_*^a \approx 0.64 \Delta t_{\text{prep}}$ . It follows that the areal density overtaken by the rarefaction wave's leading edge before the shock interaction has the same form as Eq. (23): ( $m_*^a = a_*\Delta t_*^a\rho_*$ ); however, the numerical value of  $m_*^a$  is reduced with respect to Eq. (23) by approximately 20% because of the reduction in  $\Delta t_*$  due to the ablative correction (i.e.,  $\Delta t_*^a$ ). The analysis in the previous four sections (pp. 150–157) follows without any changes, but with the premises that  $m$ ,  $m_*$ , and  $\Delta t_*$  used in the definitions of  $z$  and  $\tau$  are replaced by  $m^{(a)}$ ,  $m_*^a$ , and  $\Delta t_*^a$ , respectively, which include the ablative corrections. This leads to the following shape function from Eq. (63):

$$\hat{S} = \left[ \frac{m_*^a}{m^{(a)}} \right]^\delta, \quad (68)$$

where  $\delta \approx 1.315$  for a flat prepulse with an applied pressure that vanishes right after the prepulse end.

Another important effect occurring in laser-accelerated targets is that of residual heating of the ablation front. When the laser power is lowered (or turned off) at the end of the prepulse  $t = \Delta t_{\text{prep}}$ , the heat stored in the coronal plasma continues to flow toward the ablation front. Because of the finite heat capacity of the corona, the ablation pressure does not vanish instantaneously when the laser is turned off. Instead the ablation pressure decays in time approximately following a temporal power law:

$$P_a(t < \Delta t_{\text{prep}}) = p_*, \quad P_a(t > \Delta t_{\text{prep}}) = p_* \left( \frac{\Delta t_{\text{prep}}}{t} \right)^n. \quad (69)$$

The power index  $n$  can be determined by fitting Eq. (69) with the results of 1-D simulations using the ICF code *LILAC*.<sup>31</sup> Figures 95.13(a) and 95.13(b) compare the decay of the ablation pressures from *LILAC* (solid lines) with Eq. (69) for a 100-ps prepulse inducing a 26-Mbar ablation pressure [Fig. 95.13(a)] and a 300-ps prepulse inducing a 33-Mbar pressure [Fig. 95.13(b)] on a cryogenic DT slab of 350- $\mu\text{m}$  thickness. The power indices in Eq. (69) that fit the simulation results are  $n \approx 2$  for the 100-ps prepulse [dashed line in 95.13(a)] and  $n \approx 3$  for the 300-ps prepulse [dashed line in 95.13(b)]. It is important to notice that when the ablation pressure depends on the ratio  $t/\Delta t_{\text{prep}}$ , the resulting boundary conditions [discussed in **The General Problem of the Decaying Shock** (p. 151)] depend exclusively on the dimensionless time  $\tau = t/\Delta t_*$  and the adiabat index  $\gamma$ . Indeed, one can substitute

$$\frac{t}{\Delta t_{\text{prep}}} = \frac{\tau}{\tau_0(\gamma)}, \quad \tau_0(\gamma) = \sqrt{2\gamma/(\gamma-1)} - 1 \quad (70)$$

into Eq. (69) and conclude that the appropriate boundary condition for the dimensionless applied pressure can be cast in the following form:

$$\hat{p}(z=0, \tau < \tau_0) = 1, \quad \hat{p}(z=0, \tau > \tau_0) = \left(\frac{\tau_0}{\tau}\right)^n. \quad (71)$$

It follows that for a given value of  $\gamma$  and power index  $n$ , a single numerical simulation provides the universal function  $\hat{S}(z, n)$ . As recognized in **Self-Similar Solution** (pp. 153–154), the asymptotic solution becomes self-similar when  $n > 0.78$ ; however, the transition to a self-similar form occurs at large  $z \gg 1$  (i.e.,  $m \gg m_*$ ), while the interesting range of  $z$  for ICF applications is typically below 10. In this case, it is important to determine the adiabat shape before the transition to a self-similar profile. For this purpose, we carry out the numerical solution of Eqs. (25), with boundary conditions [Eq. (71)] and different  $n$ 's, to determine the corrections caused by a finite time decay of the pressure within the interval  $1 < z < 10$ . For simplicity, we have maintained a power law fit for  $\hat{S}$  and calculated the power index for  $n$  varying in the range of 2–6 (Table 95.I). For  $n = 2$  and 3, the numerical solution yields an adiabat shape that can be approximated with the following power laws:

$$\hat{S}[m^{(a)} > m_*^a, n=3] \approx \left[\frac{m_*^a}{m^{(a)}}\right]^{1.13}, \quad (72)$$

$$\hat{S}[m^{(a)} > m_*^a, n=2] \approx \left[\frac{m_*^a}{m^{(a)}}\right]^{1.05}.$$

Observe that the power indices are somewhat less than  $\delta = 1.315$  [Eq. (63)] derived in the case of a sudden decrease in pressure (i.e.,  $n \rightarrow \infty$ ). The fact that the adiabat shape is not as steep as in the case of a sudden decrease in pressure should not be surprising since the residual applied pressure sustains the shock, preventing its rapid decay. As expected, the value of  $\delta$  increases with  $n$  and reaches the asymptotic value  $\delta = 1.315$  for  $n \rightarrow \infty$ . This concludes the theoretical analysis of the adiabat

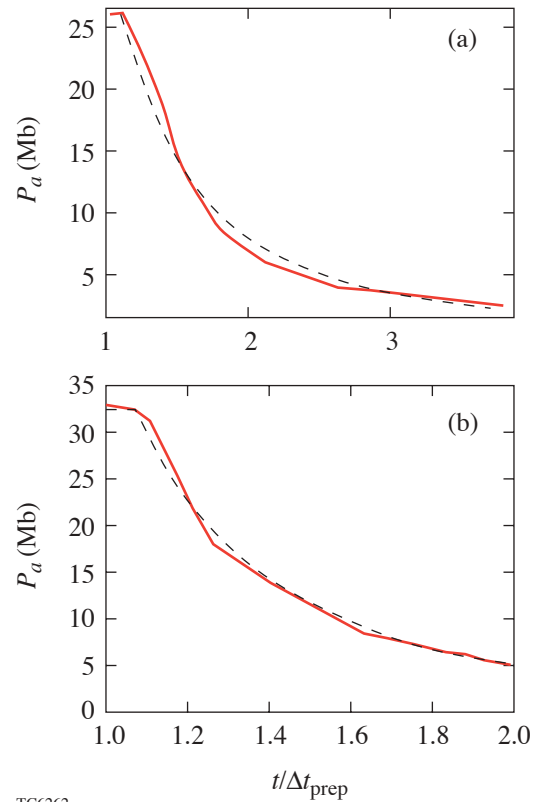


Figure 95.13

A fit of the ablation-pressure time decay from *LILAC* (solid) to a power law (dashed) for (a) a 100-ps prepulse and (b) a 300-ps prepulse.

Table 95.I: Adiabatic-shape power indices as a function of the prepulse pressure time-decay power index.

$n$	$\delta$
2	1.05
3	1.13
4	1.2
6	1.25
$\infty$	1.315

shape. The next step is to derive a set of simple formulas that can be conveniently used to design ICF-capsule or planar-foil experiments with adiabat profiles shaped by a decaying shock.

### Prepulse Design Formulas for DS Shaping

Starting from the adiabat shape derived in the previous sections, it is possible to derive some simple formulas relating the laser prepulse and foot pressure/intensity, the prepulse and duration, and the desired values of the outer- and inner-surface adiabats. It is clear that the prepulse pressure initially determines the front surface adiabat; however, since the ablation front advances inside the target with the ablation velocity, the ablation-front adiabat is typically a function of time. It is therefore important to specify a reference time at which the ablation-front adiabat is determined and optimized. Since the acceleration phase starts a short time after the shock breakout, we choose to optimize the adiabat shape at shock breakout with the intent to induce the largest-possible outer-surface adiabat during the acceleration phase. It is also important to notice that for a constant pressure prepulse, the outer-surface adiabat is constant for  $0 < m < m_*$  and decays for  $m > m_*$ .

Using the standard definition for the normalized adiabat  $\alpha \equiv P(\text{Mbar})/2.18\rho(\text{g/cm}^3)^{5/3}$ , one can easily determine the ablation pressure required to induce the desired outer-surface adiabat:

$$P_a(\text{Mbar}) = 19.6 \left( \frac{\alpha_{\text{out}}}{9} \right) \left[ \frac{\rho_0(\text{g/cm}^3)}{0.25} \right]^{1.67}, \quad (73)$$

where  $\rho_0$  is the initial shell density and the value  $\alpha_{\text{out}} = 9$  has been chosen as a typical desired value of the ablation-front

adiabat. Here, the density of  $0.25 \text{ g/cm}^3$  refers to the uncompressed DT ice. The laser intensity required to drive the ablation pressure in Eq. (73) can be derived by the standard relation  $P_a(\text{Mbar}) = 40 [I_{15}/\lambda(\mu\text{m})]^{2/3}$ , where  $I_{15}$  is the laser intensity in units of  $10^{15} \text{ W/cm}^2$ . This relation is valid for steady-state laser absorption and needs to be used with caution, as discussed later in this section. The prepulse duration can be derived from the adiabat shape and the design values of the outer- and inner-surface adiabats. Using Eq. (72), one can write

$$\frac{\alpha_{\text{out}}}{\alpha_{\text{in}}} = \left( \frac{m_{\text{shell}}^a}{m_*^a} \right)^\delta, \quad (74)$$

where  $m_{\text{shell}}^a = m_{\text{shell}}(0) - m_a^{\text{prep}}$  is the total shell areal density left after the prepulse and  $\delta \approx 1$  as for typical prepulses with  $\Delta t_{\text{prep}} \leq 300 \text{ ps}$ . A straightforward manipulation of Eq. (74) yields the following form of the required prepulse duration:

$$\begin{aligned} \Delta t_{\text{prep}}(\text{ps}) &= 180 \left[ \frac{d_{\text{shell}}(\mu\text{m})}{100} \right] \left[ \frac{0.25}{\rho_0(\text{g/cm}^3)} \right]^{0.33} \\ &\times \left( \frac{9}{\alpha_{\text{out}}} \right)^{0.5 + \frac{1}{\delta}} \left( \frac{\alpha_{\text{inn}}}{3} \right)^{\frac{1}{\delta}} \frac{3^{1 - \frac{1}{\delta}}}{1 - \epsilon_a}, \end{aligned} \quad (75)$$

where  $d_{\text{shell}}$  is the initial shell thickness and  $\epsilon_a = M_a^{\text{prep}} [2.23 - 1.54(\alpha_{\text{inn}}/\alpha_{\text{out}})^{1/\delta}]$  represents the ablative correction, which is typically  $\epsilon_a < 0.2$  for  $M_a^{\text{prep}} \approx 0.09$ . Equations (73) and (75) show that an arbitrarily large adiabat ratio can be induced by simply increasing the applied prepulse pressure and decreasing the prepulse duration. There are limitations, however, with regard to the magnitude of the outer-surface adiabat and the adiabat ratio. The first constraint concerns the adiabat ratio at the shock-breakout time  $\theta = \alpha_{\text{out}}/\alpha_{\text{inn}}$ . The limits of  $\theta$  are dictated by the mass ablated during the foot of the laser pulse following the prepulse. Since the adiabat is flat for  $m < m_*^a$ , the largest outer-surface adiabat (for a given inner-surface adiabat) can be achieved by tailoring the prepulse intensity and the laser foot duration in order to ablate the flat-adiabat region. This requires that

$$m_a^{\text{foot}} = m_*^a, \quad (76)$$

where  $m_a^{\text{foot}} = \dot{m}_a^{\text{foot}} \Delta t_{\text{foot}}$  is the mass ablated during the time interval between the end of the prepulse and the shock-breakout time. A similar principle is used in Ref. 18.

The interval  $\Delta t_{\text{foot}}$  can be estimated from Eq. (26a) relating the shock velocity  $\dot{z}_s$  to the shell adiabat  $\hat{S}(z) \approx 1/z^\delta$ , leading to the following shock trajectory:

$$z_s(\tau) = \left[ 1 + \left( 1 + \frac{\delta}{2} \right) \sqrt{\frac{\gamma-1}{2\gamma}} (\tau-1) \right]^{\frac{2}{2+\delta}}. \quad (77)$$

It follows that the time interval between the end of the prepulse ( $\tau = 0$ ) and the shock-breakout time can be derived from Eq. (77) by setting  $z_s = \theta^{1/\delta}$ , where  $\theta = \alpha_{\text{out}}/\alpha_{\text{inn}}$  is the desired adiabat ratio. This time interval represents the foot duration  $\Delta t_{\text{foot}}$  and depends only on the prepulse characteristics (it is independent of the foot). This is not the case in the absence of a prepulse since the foot length depends on the foot properties. In the simplest pulse shapes, the foot intensity is kept constant, such that the induced ablation pressure  $P_{\text{foot}}$  corresponds to the desired inner-surface adiabat.

It follows that the foot properties ( $\Delta t_{\text{foot}}$  and  $P_{\text{foot}}$ ) can be summarized by the following simple formulas:

$$\Delta t_{\text{foot}} = \Delta t_*^a \left[ 1 + \frac{\theta^{\frac{2+\delta}{2\delta}} - 1}{\sqrt{\frac{\gamma-1}{2\gamma}} \left( 1 + \frac{\delta}{2} \right)} \right], \quad (78a)$$

$$P_a^{\text{foot}} (\text{Mbar}) = 2.18 \alpha_{\text{inn}} \left[ \frac{\rho_0 (\text{g/cm}^3)}{0.25} \right]^{1.67}, \quad (78b)$$

where  $\Delta t_*^a \approx 0.64 \Delta t_{\text{prep}}$  for DT. Observe that, using (78a),  $\Delta t_*^a$  cancels from both sides of Eq. (76) and the maximum adiabat ratio  $\theta_*$  satisfies the following equation:

$$\left[ 1 + \frac{\theta_*^{\frac{2+\delta}{2\delta}} - 1}{\sqrt{\frac{\gamma-1}{2\gamma}} \left( 1 + \frac{\delta}{2} \right)} \right] M_a^{\text{prep}} \frac{\dot{m}_a^{\text{foot}}}{\dot{m}_a^{\text{prep}}} = 1. \quad (79)$$

Using Eqs. (66), it follows that the foot/prepulse ablation rate ratio is related to the foot/prepulse pressures and therefore adiabats through the relation  $\dot{m}_a^{\text{prep}}/\dot{m}_a^{\text{foot}} = \sqrt{\theta}$ . It is very important to notice that the steady-state ablation relations used in Eq. (66) and adopted in the current derivation are not very accurate during the prepulse where a steady state is not reached. Furthermore, high-performance target design requires the foot intensity to rise before the shock breaks out on the inner surface. This is commonly done to prevent secondary shock generation during the rise to full power, which would set the inner portion of the shell on a high adiabat. Since the total laser energy in a rising foot is larger than in a flat (constant-intensity) foot of the same starting power, it follows that the mass ablated during the rising foot is larger than for the flat foot. All these uncertainties in the calculation of the ablated mass can be heuristically accounted for by introducing a corrective factor  $\chi$  in the ratio of mass ablation rates, thus setting

$$\frac{\dot{m}_a^{\text{prep}}}{\dot{m}_a^{\text{foot}}} = \frac{\sqrt{\theta}}{\chi}, \quad (80)$$

where  $\chi > 1$  represents an enhancement with respect to the steady-state ablation rate of a flat foot. The final form of the equation governing the maximum adiabat ratio can be written in the following form:

$$\left[ 1 + \frac{\theta_*^{\frac{2+\delta}{2\delta}} - 1}{\sqrt{\frac{\gamma-1}{2\gamma}} \left( 1 + \frac{\delta}{2} \right)} \right] M_a^{\text{prep}} \frac{\chi}{\sqrt{\theta_*}} = 1, \quad (81)$$

where  $\theta_*$  is the optimized adiabat ratio. To estimate the size of the maximum adiabat ratio, we solve Eq. (81) for cryogenic DT with  $M_a^{\text{prep}} \approx 0.09$  [Eq. (67)] for both the idealized case of  $\chi = 1$  and for a more-realistic rising-foot case with  $\chi = 1.4$ . The results are given in Table 95.II. Note that the maximum adiabat ratio is lower in the rising-foot case. Because the maximum adiabat ratio is given by Eq. (81), the optimum prepulse pressure and duration are determined by Eqs. (73) and (75) upon substitutions of the maximum ratio  $\theta_*$  leading to

$$P_a^{\text{prep}} (\text{Mbar}) \approx 19.6 \alpha_{\text{inn}} \left( \frac{\theta_*}{9} \right) \left[ \frac{\rho_0 (\text{g/cm}^3)}{0.25} \right]^{1.67}, \quad (82)$$

Table 95.II: Maximum ratio of inner- to outer-surface adiabat as a function of the adiabat-shape power index for two values of  $\xi$ .

$\delta$	$\theta_*$	
	$\chi = 1.0$	$\chi = 1.4$
1.0	7.6	5.5
1.1	9.6	6.7
1.2	12.0	8.2

$$\Delta t_{\text{prep}} (\text{ps}) = 42 \times 3^{2-\frac{2}{\delta}} \left[ \frac{d_{\text{shell}} (\mu\text{m})}{100} \right] \times \left[ \frac{0.25}{\rho_0 (\text{g/cm}^3)} \right]^{0.33} \left( \frac{9}{\theta_*} \right)^{0.5+\frac{1}{\delta}} \left( \frac{3}{\alpha_{\text{inn}}} \right)^{0.5}, \quad (83)$$

where  $\epsilon_a$  has been set approximately equal to 0.18 in accordance with typical adiabat ratios of 5 to 10 and  $\delta$  is provided in Table 95.I ( $\delta \approx 1.05$  and  $\delta \approx 1.13$  for prepulses in the 100-ps and 300-ps range, respectively).

The mass-ablated  $m_a^{\text{tot}} = m_a^{\text{prep}} + m_a^{\text{foot}}$  during the prepulse and the foot of the laser pulse can be easily determined by using Eq. (80), leading to

$$m_a^{\text{tot}} = \dot{m}_a^{\text{prep}} \Delta t_{\text{prep}} \left( 1 + \frac{\chi}{\sqrt{\theta}} \frac{\Delta t_{\text{foot}}}{\Delta t_{\text{prep}}} \right). \quad (84)$$

The foot/prepulse-length ratio in Eq. (84) can be derived from Eq. (78), and, after a straightforward manipulation, the total ablated mass fraction can be written in the following form:

$$\frac{m_a^{\text{tot}}}{m_{\text{shell}}} = \frac{1}{1 + \omega_a} \times \left\{ \omega_a + \left[ 1 + \frac{\theta^{\frac{2+\delta}{2\delta}} - 1}{\sqrt{\frac{\gamma-1}{2\gamma}} \left( 1 + \frac{\delta}{2} \right)} \right] M_a^{\text{prep}} \frac{\chi}{\theta^{0.5+1/\delta}} \right\}, \quad (85a)$$

where

$$\omega_a = \frac{M_a^{\text{prep}}}{\theta^{\frac{1}{\delta}}} \frac{1.24}{1 - 2.23 M_a^{\text{prep}}}. \quad (85b)$$

Equation (85) is valid for any prepulse and can be simplified for the optimized prepulse defined by Eq. (81), leading to

$$\frac{m_a^{\text{tot}}}{m_{\text{shell}}} = \frac{1}{1 + \omega_a(\theta_*)} \left[ \omega_a(\theta_*) + \frac{1}{\theta_*^{1/\delta}} \right], \quad (86)$$

where  $\theta_*$  is the optimized adiabat ratio satisfying Eq. (81). Observe that Eq. (86) does not depend directly on the corrective factor  $\chi$ ; however, it does depend on  $\chi$  through the optimized adiabat ratio and can be conveniently used to determine the corrective factor  $\chi$  when compared with numerical simulation. A single iteration is usually adequate to calculate  $\chi$ . One starts by guessing a value of  $\chi \sim 1$ , then designs the optimized prepulse and foot by solving Eq. (81) to find  $\theta_*$ ; Eqs. (82) and (83) to find  $\Delta t_{\text{prep}}$  and  $P_a^{\text{prep}}$ ; Eqs. (78a) and (78b) to find  $\Delta t_{\text{foot}}$  and  $P_a^{\text{foot}}$ ; and Eq. (86) to find the ablated mass fraction during the prepulse + foot. The pulse (prepulse + foot) is then simulated with a one-dimensional code, and the fraction of ablated mass is extracted at shock breakout from the simulation output. If this fraction is larger/smaller than the one predicted by Eq. (86), then one increases/decreases  $\chi$  until Eqs. (81) and (86) yield the same value of the ablated fraction from the simulation. One then recalculates the prepulse and foot properties with the new value of  $\chi$ . Typically, one adjustment of  $\chi$  is sufficient to produce highly accurate results since the difference between simulated values and desired design parameters is negligible. For typical high-performance target designs,<sup>18</sup> the ablated mass fraction [Eq. (86)] during the prepulse + foot is in the 20% range. As shown in the next section, this pulse design technique seems to be quite accurate, general, and applicable to different foot and prepulse shapes.

### Simplified Adiabat Profiles and Comparison with *LILAC*

After including the “nonideal” effects of mass ablation and residual ablation pressure, it is useful to carry out a detailed comparison between the theoretical results of the previous sections and the predictions of the 1-D ICF code *LILAC*<sup>31</sup> including all the relevant ICF physics. All the *LILAC* runs are carried out selecting the Thomas–Fermi equation of state. Different choices of the equation of state do not significantly alter the adiabat shape as long as the prepulse is tuned in order to induce the desired inner-surface adiabat.

To carry out a meaningful comparison of the adiabat shapes, it is convenient to rewrite the adiabat shape function [Eq. (68)] in a form that can be easily compared with the output of *LILAC*. The first obstacle is in the accurate determination of the terms  $m^{(a)}$  and  $m_*^a$  in Eq. (68), which are typically hard to extract from *LILAC* output. This can be avoided by rewriting Eq. (68) using the full areal-density coordinate  $m = m^{(a)} + m_a^{\text{prep}}$ . Note that the ratio  $\mu_a \equiv m_a^{\text{prep}}/m_*^a$  is significantly smaller than unity. For DT and a laser of  $\lambda = 0.35 \mu\text{m}$ ,

$$\mu_a = \frac{\dot{m}_a \Delta t_{\text{prep}}}{\Delta t_*^a \rho_* a_*} \approx 1.54 M_a^{\text{prep}} \approx 0.14. \quad (87)$$

Since it is much smaller than unity, one can simplify Eq. (68) using  $\mu_a$  as an expansion parameter. A straightforward manipulation leads to the following adiabat shape function including first-order corrections in  $\mu_a$ :

$$\hat{S}(m > m_*^{\text{tot}}) \approx \left( \frac{m_*^{\text{tot}}}{m} \right)^{\delta_a} \left[ 1 + \delta \mu_a f(\eta) + \mathcal{O}(\epsilon_a^2) \right], \quad (88a)$$

where  $m_*^{\text{tot}} = m_*^a + m_a^{\text{prep}}$  and  $\eta = m/m_*^{\text{tot}}$  varies between  $\eta_{\min} = 1$  and  $\eta_{\max} = m_{\text{shell}}/m_*^{\text{tot}}$ , where  $m_{\text{shell}}$  is the total shell areal density. The function  $f(\eta)$  and the power index  $\delta_a$  can be cast in the following form:

$$f(\eta) = \frac{\eta_{\max} - 1}{\eta_{\max} \log \eta_{\max}} \log \eta + \frac{1}{\eta} - 1, \quad (88b)$$

$$\delta_a = \delta \left( 1 + \epsilon_a \frac{\eta_{\max} - 1}{\eta_{\max} \log \eta_{\max}} \right). \quad (88c)$$

It is important to observe that the function  $f(\eta)$  vanishes at both  $\eta = 1$  and  $\eta = \eta_{\max}$  and its maximum varies between 0.16 and 0.24 for typical values of  $5 < \eta_{\max} < 10$ . It follows that the  $\mu_a f(\eta)$  term in Eq. (88a) can be neglected and the adiabat shape for DT can be written as a simple power law:

$$\hat{S}(m > m_*^{\text{tot}}) \approx \left( \frac{m_*^{\text{tot}}}{m} \right)^{\delta_a} \approx \left( \frac{m_*^{\text{tot}}}{m} \right)^{1.062\delta}, \quad (89)$$

where the relation  $\delta_a \approx 1.062\delta$  has been used in view of the fact that  $\delta_a$  is approximately independent of  $\eta_{\max}$  as it varies between  $\delta_a \approx 1.07\delta$  for  $\eta_{\max} = 10$  and  $\delta_a \approx 1.055\delta$

for  $\eta_{\max} = 5$ . Using Eq. (89), the adiabat profile can be written as a convenient function of the full areal-density coordinate  $m$  and the initial shell areal density  $m_{\text{shell}}$ :

$$\alpha \approx \alpha_{\text{inn}} \left( \frac{m_{\text{shell}}}{m} \right)^{1.062\delta}. \quad (90)$$

Obviously, Eq. (90) can be easily compared with *LILAC* output since the inner-surface adiabat and the full areal density are readily available, while the values of  $\delta$  are given in Table 95.I for different prepulse durations.

We consider two prepulses with 100-ps and 300-ps duration and 300-TW/cm<sup>2</sup> intensity applied to a 200- $\mu\text{m}$  and 500- $\mu\text{m}$  planar DT foil, respectively. From *LILAC* output we immediately find that  $\alpha_{\text{inn}} = 0.85$  and 1.18 for the 100-ps and 300-ps prepulses, respectively. According to the theory and Table 95.I, the adiabat shapes can be approximated as

$$\alpha(\sim 100 \text{ ps}) \approx \alpha_{\text{inn}} \left( \frac{m_{\text{shell}}}{m} \right)^{1.12}, \quad (91)$$

$$\alpha(\sim 300 \text{ ps}) \approx \alpha_{\text{inn}} \left( \frac{m_{\text{shell}}}{m} \right)^{1.20},$$

where the symbol  $\sim$  indicates that the two adiabat profiles can be used for prepulses in the 100-ps and 300-ps range, respectively. Figure 95.14 shows the adiabat profiles versus the normalized Lagrangian coordinate  $m/m_{\text{shell}}$  from *LILAC* (solid) and from Eqs. (91) (dashed) for the two prepulses. The good agreement between theory and simulations indicates that Eqs. (90) and (91) can indeed be used to accurately determine the adiabat profiles of typical ICF targets.

The next step is to compare the maximum obtainable adiabat ratio provided by Eq. (81) with *LILAC* simulations. We consider an 85- $\mu\text{m}$  solid DT planar foil in order to simulate a typical OMEGA cryogenic shell and focus on the simple case of a flat-laser-foot intensity. The mass ablation enhancement factor  $\chi$  is initially set equal to unity and then adjusted to  $\chi = 0.85$  in order to recover the mass-ablated fraction of 13% as indicated by the *LILAC* simulations. We choose an inner-surface adiabat of  $\alpha_{\text{inn}} = 1$  and determine the maximum adiabat ratio through Eq. (81), leading to  $\theta_* \approx 10$ . Equations (75) and (78) yield prepulse and foot durations of 60 ps and 1571 ps, respectively. The predicted shock-breakout time is then

$t_s = \Delta t_{\text{prep}} + \Delta t_{\text{foot}} = 1631$  ps. The required ablation pressure to induce an outer-surface adiabat of 10 is 22 Mbar. The laser prepulse intensity required to induce such an ablation pressure in 60 ps has been determined with *LILAC* to be  $I_L^{\text{prep}} \approx 450$  TW/cm<sup>2</sup>. The foot ablation pressure corresponding to an inner-surface adiabat  $\alpha_{\text{inn}} = 1$  is 2.2 Mbar, requiring, according to *LILAC*, a foot intensity of 6.9 TW/cm<sup>2</sup>. The solid curve in Fig. 95.15 represents the laser pulse profile used in *LILAC* simulations.

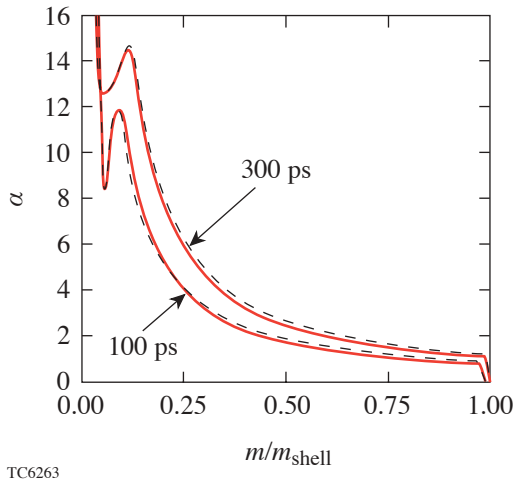


Figure 95.14  
A comparison of the adiabat shapes for two *LILAC* simulations with 100-ps and 300-ps prepulses (solid lines) to the formulas generated in Eqs. (91) (dashed lines).

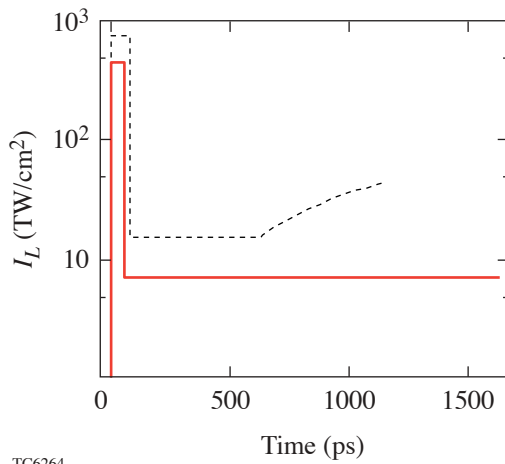


Figure 95.15  
Optimal laser intensity history from *LILAC* for an 85- $\mu\text{m}$  solid-DT planar foil with design specifications of  $\alpha_{\text{inn}} = 1$  and flat-laser-foot intensity (solid) and  $\alpha_{\text{inn}} = 2$  and rising-laser-foot intensity (dashed).

Figure 95.16(a) shows the adiabat profile at shock breakout obtained from *LILAC* using the pulse described above: a 60-ps, 450-TW/cm<sup>2</sup> prepulse followed by a 6.9-TW/cm<sup>2</sup> foot. The shock-breakout time  $t^{\text{shock}}$  according to *LILAC* is about 1632 ps, in excellent agreement with the theoretical prediction of 1631 ps. The theoretical adiabat profiles [the dashed curve provided by the first of Eq. (91)] is also in agreement with *LILAC* results, as is the prediction of the maximum adiabat ratio as indicated by the fact that the flat-adiabat region preceding the adiabat decay is completely ablated off at shock breakout. The pressure profile at shock breakout is approximately flat [Fig. 95.16(b)] with a value of about 2.2 to 2.3 Mbar in compliance with the design requirement. The ablated mass fraction is given by the abscissa of the vertical dotted line in Fig. 95.16, indicating an ablated fraction of about 13%, in agreement with the result of Eq. (86) yielding 12.6%.

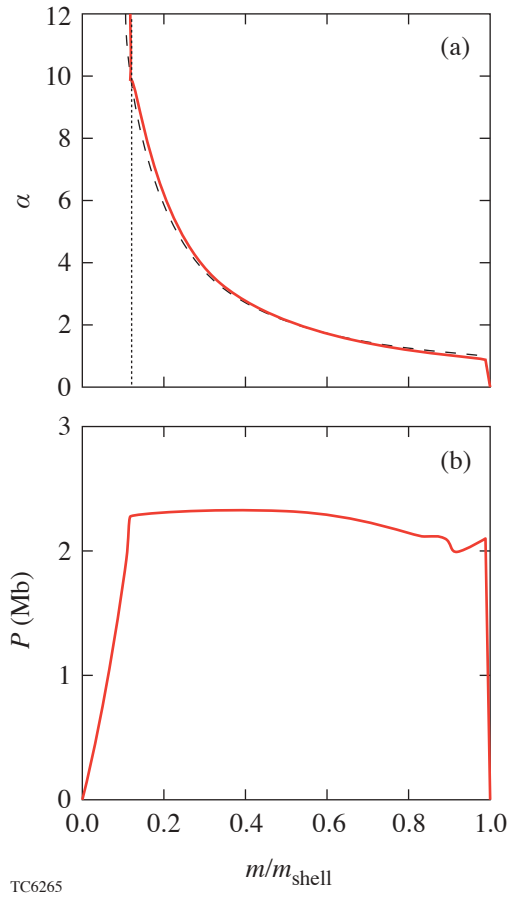


Figure 95.16  
(a) Comparison of the *LILAC* adiabat profile at shock breakout for the flat-foot laser pulse given by the solid line in Fig. 95.15 with the theoretical prediction of Eq. (91) (dashed line). The ablated mass fraction from *LILAC* is shown by the vertical dotted line. (b) Pressure profile at shock breakout for the target and pulse in Fig. 95.16(a).

To apply the theory to more-realistic designs, we have also carried out the optimization for the case of a rising-foot intensity and higher inner-surface adiabat. We consider a typical OMEGA cryogenic capsule design with  $\alpha_{\text{inn}} \approx 2$  and a laser foot intensity that is flat over half its length and then linearly ramped up to three times its initial intensity at shock breakout. The corrective factor  $\chi$  can be determined in one iteration to be about 1.3, leading to an ablated fraction of 18% [from Eq. (86)], an adiabat ratio of 6.4 [Eq. (81)], and an outer-surface adiabat of 12.8.

The prepulse pressure and duration from Eqs. (82) and (83) are approximately 28 Mbar and 79 ps, respectively. The prepulse intensity required to induce such an ablation pressure in 79 ps is found with *LILAC* to be about 750 TW/cm<sup>2</sup>. Equations (78) yield a foot duration of 1089 ps, leading to a shock-breakout time of 1169 ps, and a starting foot pressure of 4.3 Mbar. The foot is split into a 544-ps flat foot with a 15-TW/cm<sup>2</sup> laser intensity followed by a 544-ps linear ramp to 45 TW/cm<sup>2</sup>. The dashed curve in Fig. 95.15 represents the laser pulse used in *LILAC* simulations.

Figure 95.17(a) shows the adiabat shape at shock breakout obtained with *LILAC* (solid line) with an inner-surface adiabat of about 2 and the theoretical prediction from Eq. (91). According to *LILAC*, the outer-surface adiabat is about 13 and the shock-breakout time is 1160 ps, in excellent agreement with the theoretical predictions of 12.8 and 1169 ps, respectively. Figure 95.17(b) shows the pressure profile at shock breakout. The characteristic pressure bump on the left is due to the intensity ramp, while the flat region on the right at about 4.3 Mb is due to the flat portion of the foot.

It is important to observe that the laser intensity required to generate the desired prepulse ablation pressure is significantly larger than the one predicted by steady ablation formulas. Indeed, according to the steady ablation theory

$$P_a(\text{Mbar}) \approx 40 \left[ \frac{I_L^{15}}{\lambda(\mu\text{m})} \right]^{2/3}, \quad (92)$$

the intensity required to induce 28 Mbar of pressure is approximately 205 TW/cm<sup>2</sup>. Instead, the 79-ps prepulse described above required 750 TW/cm<sup>2</sup> to generate 28 Mbar. This discrepancy comes about because the ablation process does not reach a steady state in 79 ps. Furthermore, a fast ramp of the laser intensity during the prepulse causes a hydrodynamic decoupling

between the shell and the laser with the result that most of the prepulse laser energy goes into heating the coronal plasma instead of driving the required strong shock. This explains why a very large increase in laser intensity has only a modest effect on the prepulse hydrodynamics. If one takes into account the limitations of the laser system with regard to the maximum power and power ramping rate, then the maximum prepulse pressure and outer-surface adiabat are further reduced. All of these effects need to be accounted for on a case-by-case basis through careful one-dimensional simulations.

It is important to notice that Eqs. (78) and (81)–(83) should be used with caution in determining the optimal pulse parameters when the resulting laser pulse is limited by either the laser peak power or rise time. When the prepulse is not flat, Eq. (83)

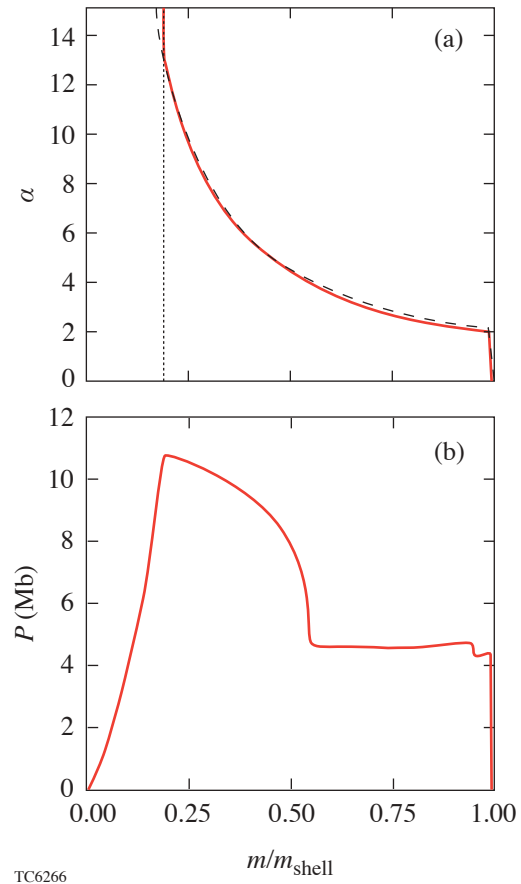


Figure 95.17

(a) Comparison of the *LILAC* adiabat profile at shock breakout for the rising-foot laser pulse given by the dashed line in Fig. 95.15 with the theoretical prediction of Eq. (91) (dashed line). The ablated mass fraction from *LILAC* is shown by the vertical dotted line. (b) Pressure profile at shock breakout for the target and pulse in Fig. 95.17(a).

for a square prepulse needs to be adjusted to reproduce the same total prepulse energy. In this case, the theoretical results are not as accurate as in the case of a square pulse and need to be refined by numerical simulations. As an example, we consider a typical OMEGA cryogenic spherical target that has an outer radius of  $430 \mu\text{m}$  and a thickness of  $85 \mu\text{m}$ . A square prepulse is designed for an  $\alpha_{\text{inn}} \approx 2$  using Eqs. (81)–(83) with an adjusted  $\chi = 1.42$  in order to obtain an ablated mass fraction of 21%, as indicated by *LILAC* simulations. The maximum adiabat ratio follows from Eq. (81) leading to  $\theta_* = 5.9$  with an outer-surface adiabat of about 11.8. According to Eqs. (78)–(83), the prepulse duration is about 90 ps with a foot of 1083 ps. The foot again is divided into a flat portion lasting half of the foot length followed by a linear intensity ramp to three times the initial intensity. If one takes into account the OMEGA power ramping rate limit of approximately 10 TW over 50 ps, then the prepulse can be divided into a 70-ps linear ramp to 14 TW followed by a 55-ps flattop. This is approximately equivalent to a 90-ps square pulse. The foot starts at 0.36 TW for 542 ps and a linear ramp to 1.08 TW for another 542 ps. The curve in Fig. 95.18 represents the laser pulse (prepulse + foot) used in *LILAC* simulations.

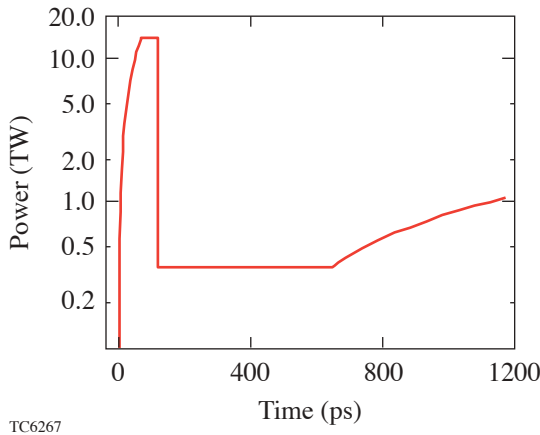


Figure 95.18  
Optimal laser intensity history from *LILAC* for a typical OMEGA cryogenic DT spherical capsule with design specification of  $\alpha_{\text{inn}} = 2$ , rising-foot intensity, and experimental power-ramping limitations.

Figure 95.19 shows the adiabat shape for the OMEGA cryogenic capsule simulated with *LILAC* using the pulse described above. Notice that the outer-surface adiabat is about 12 and the ablated mass is about 21%, in agreement with the theoretical prediction for an equivalent square prepulse. The adiabat shape from *LILAC* (solid line) is also in good agreement with Eq. (91), indicating that the theory applies to spherical shells as well as planar foils.

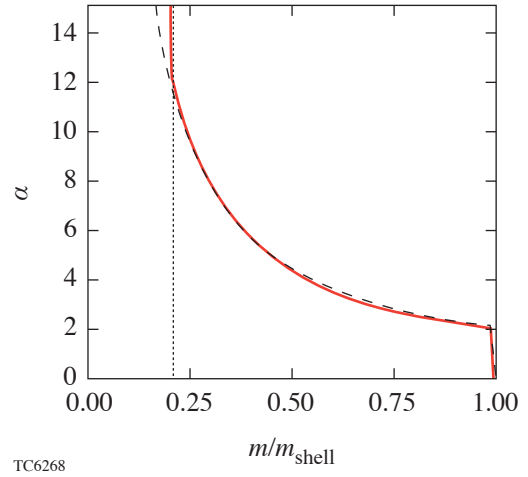


Figure 95.19  
Comparison of the *LILAC* adiabat profile at shock breakout for the laser pulse shown in Fig. 95.18 with the theoretical prediction of Eq. (91). The ablated mass fraction from *LILAC* is shown by the vertical dotted line.

**Conclusions**

The adiabat profile induced by a decaying shock is calculated including the effects of mass ablation and residual ablation pressure. The adiabat shape follows a simple power law of the shell areal density  $m$ :

$$\alpha = \alpha_{\text{inn}} \left( \frac{m_{\text{shell}}}{m} \right)^{\delta_a}, \tag{93}$$

where  $\alpha_{\text{inn}}$  is the inner-surface adiabat,  $m_{\text{shell}}$  is the total initial shell areal density, and  $m$  is the shell’s local areal density. The power index  $\delta_a$  varies from 1.12 for a 100-ps prepulse to 1.20 for a 300-ps prepulse. The calculated profile reproduces the simulation results with only a few-percent error, and it can be used to design the optimum prepulse, which leads to the maximum adiabat ratio between the inner- and outer-shell surfaces. Our theoretical results on the ideal adiabat shape without ablation are in qualitative agreement with other published work but show improved accuracy when compared with the numerical solutions.

**ACKNOWLEDGMENT**

This work was supported by the U.S. Department of Energy Office of Inertial Confinement Fusion under Cooperative Agreement No. DE-FC03-92SF19460, the University of Rochester, and the New York State Energy Research and Development Authority. The support of DOE does not constitute an endorsement by DOE of the views expressed in this article.

## REFERENCES

1. J. D. Lindl, *Inertial Confinement Fusion: The Quest for Ignition and Energy Gain Using Indirect Drive* (Springer-Verlag, New York, 1998).
2. Lord Rayleigh, in *Scientific Papers* (Cambridge University Press, Cambridge, England, 1900), Vol. II, pp. 200–207.
3. Y. Kato *et al.*, Phys. Rev. Lett. **53**, 1057 (1984); Laboratory for Laser Energetics LLE Review **33**, 1, NTIS document No. DOE/DP/40200-65 (1987). Copies may be obtained from the National Technical Information Service, Springfield, VA 22161.
4. S. Skupsky, R. W. Short, T. Kessler, R. S. Craxton, S. Letzring, and J. M. Soures, J. Appl. Phys. **66**, 3456 (1989).
5. R. H. Lehmburg, A. J. Schmitt, and S. E. Bodner, J. Appl. Phys. **62**, 2680 (1987).
6. P. W. McKenty, V. N. Goncharov, R. P. J. Town, S. Skupsky, R. Betti, and R. L. McCrory, Phys. Plasmas **8**, 2315 (2001).
7. S. E. Bodner, Phys. Rev. Lett. **33**, 761 (1974).
8. H. Takabe *et al.*, Phys. Fluids **28**, 3676 (1985).
9. J. Sanz, Phys. Rev. Lett. **73**, 2700 (1994).
10. R. Betti, V. N. Goncharov, R. L. McCrory, and C. P. Verdon, Phys. Plasmas **5**, 1446 (1998).
11. A. R. Piriz, J. Sanz, and L. F. Ibañez, Phys. Plasmas **4**, 1117 (1997).
12. M. C. Herrmann, M. Tabak, and J. D. Lindl, Nucl. Fusion **41**, 99 (2001).
13. A. Kemp, J. Meyer-ter-Vehn, and S. Atzeni, Phys. Rev. Lett. **86**, 3336 (2001).
14. R. Betti, K. Anderson, V. N. Goncharov, R. L. McCrory, D. D. Meyerhofer, S. Skupsky, and R. P. J. Town, Phys. Plasmas **9**, 2277 (2002).
15. J. H. Gardner, S. E. Bodner, and J. P. Dahlburg, Phys. Fluids B **3**, 1070 (1991).
16. S. E. Bodner *et al.*, Phys. Plasmas **7**, 2298 (2000).
17. L. Phillips *et al.*, Laser Part. Beams **17**, 225 (1999).
18. V. N. Goncharov, J. P. Knauer, P. W. McKenty, P. B. Radha, T. C. Sangster, S. Skupsky, R. Betti, R. L. McCrory, and D. D. Meyerhofer, Phys. Plasmas **10**, 1906 (2003).
19. Laboratory for Laser Energetics LLE Review **94**, 91, NTIS document No. DOE/SF/19460-485 (2003). Copies may be obtained from the National Technical Information Service, Springfield, VA 22161.
20. T. J. B. Collins and S. Skupsky, Phys. Plasmas **9**, 275 (2002).
21. N. Metzler, A. L. Velikovich, and J. H. Gardner, Phys. Plasmas **6**, 3283 (1999).
22. N. Metzler *et al.*, Phys. Plasmas **9**, 5050 (2002).
23. Ya. B. Zel'dovich and Yu. P. Raizer, *Physics of Shock Waves and High-Temperature Hydrodynamic Phenomena*, edited by W. D. Hayes and R. F. Probstein (Dover Publications, Mineola, NY, 2002), pp. 820–839.
24. G. I. Barenblatt, *Scaling, Self-Similarity, and Intermediate Asymptotics*, Cambridge Texts in Applied Mathematics (Cambridge University Press, Cambridge, England, 1996).
25. V. B. Adamskii, Sov. Phys.-Acoust. **2**, 1 (1956).
26. A. I. Zhukov and Ia. M. Kazhdan, Sov. Phys.-Acoust. **2**, 375 (1956).
27. W. Häfele, Z. Naturforschg. **10a**, 1006 (1955).
28. S. v. Hoerner, Z. Naturforschg. **10a**, 687 (1955).
29. C. E. Max, C. F. McKee, and W. C. Mead, Phys. Fluids **23**, 1620 (1980); Phys. Rev. Lett. **45**, 28 (1980).
30. W. M. Manheimer, D. G. Colombant, and J. H. Gardner, Phys. Fluids **25**, 1644 (1982).
31. J. Delettrez and E. B. Goldman, Laboratory for Laser Energetics Report No. 36, University of Rochester (1976).